INSTRUMENTATION OF SOLAR HEATING AND COOLING SYSTEMS AT COLORADO STATE UNIVERSITY

Peter R. Armstrong
Colorado State University
Fort Collins, CO 80523

Five test buildings, representing single family dwellings, have been built and operated at the Colorado State University Solar Village beginning in 1974. A variety of solar cooling, space heating and domestic water heating systems have been evaluated in these buildings. This paper describes the evaluation objectives, the kinds of systems monitored and the kinds of data collected, the equipment used to measure and record the data, and the installation and calibration procedures which have been established. Procedures and equipment that have been found to give high quality data at reasonable cost are emphasized. Many of the standard instrumentation topics which are familiar to most workers involved in solar performance monitoring (e.g. pyranometers) are not discussed at all. This is not meant to slight their importance; we simply have nothing new to say on these topics.

Most of the information presented here comes from two recent CSU reports [1,2]. The CSU projects have been supported by the Department of Energy, whose support is gratefully acknowledged.

Further information on these projects can be obtained by ordering the cited reports or other publications currently on the Solar Energy Applications Laboratory publications list. The publications list is available on request. Parts of this paper are excerpts from the final report [3] of a project sponsored by the Electric Power Research Institute whose support is also gratefully acknowledged.

Types of Data

The overall objective of performance monitoring at CSU is to obtain data that allow the thermal behavior of each major component to be accurately characterized. Occasionally it is necessary to study a component in greater detail, for example to measure the saturation temperatures and pressures in an asorption chiller, however these studies are peripheral to the main objective. By obtaining a continuous record of the operating conditions and heat flows in and out of the major components it is possible to characterize each component as a "black box." One can then verify a mathematical or numerical model of the component and determine whether the parameters (heat transfer coefficients, pumping rates, etc.) characterizing the component deviate from the values specified in the design. One can also learn about the interactions between components that are not always apparent from simulation models. For example, modeling a discrete state controller as a proportional controller is a reasonable approximation in some cases but not in others. Finally one can report performance of the overall system as well as performance of individual components along with the average operating conditions. It is often useful to report these performance data for different periods such as a day, a month, or an entire heating or cooling season.

Some examples of the useful forms in which data from the CSU projects have been reported are illustrated in Figures 1-5. Figure 1 shows the instantaneous cooling performance, at half hour intervals, of an air-to-air heat pump used to "cold-charge" storage during the electric utility's peak hours. Figure 2 shows the evolution of rock bed temperature profiles during a corresponding period and beyond into the discharge period as well. Figure 3 illustrates how the parameters of a particular component (the solar collector array) may be estimated from actual operating data. The operating conditions, T_a, T_i, and I_t, are measured every ten minutes along with the rate of heat removal, q, per unit collector area. From these data the parameters of the Hottel-Whillier collector model:

$$\text{efficiency} = \frac{q}{I_t} = F_R\tau\alpha - F_R U_L\ (T_i - T_a)$$

may be obtained by a least squares fit.

The Hottel-Whillier model may or may not be adequate depending on one's modelling needs. The parameters of more realistic models, for example models that contain a thermal radiation term:

$$\frac{q}{I_t} = F_R\tau\alpha - F_R U_C\ (T_i - T_a) + F_R\sigma\varepsilon\ T_i^4 - T_a^4)$$

Figure 1.

One half hour heat pump data.

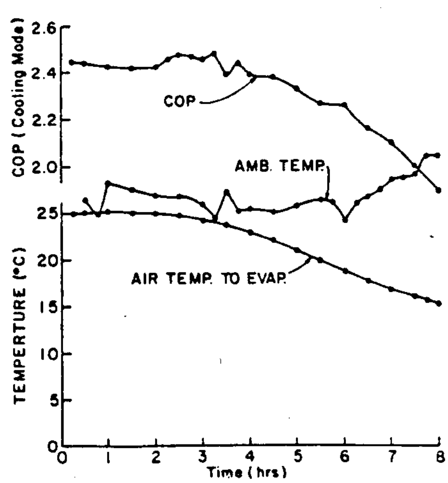

Figure 2.
Two-hourly storage temperature profiles.

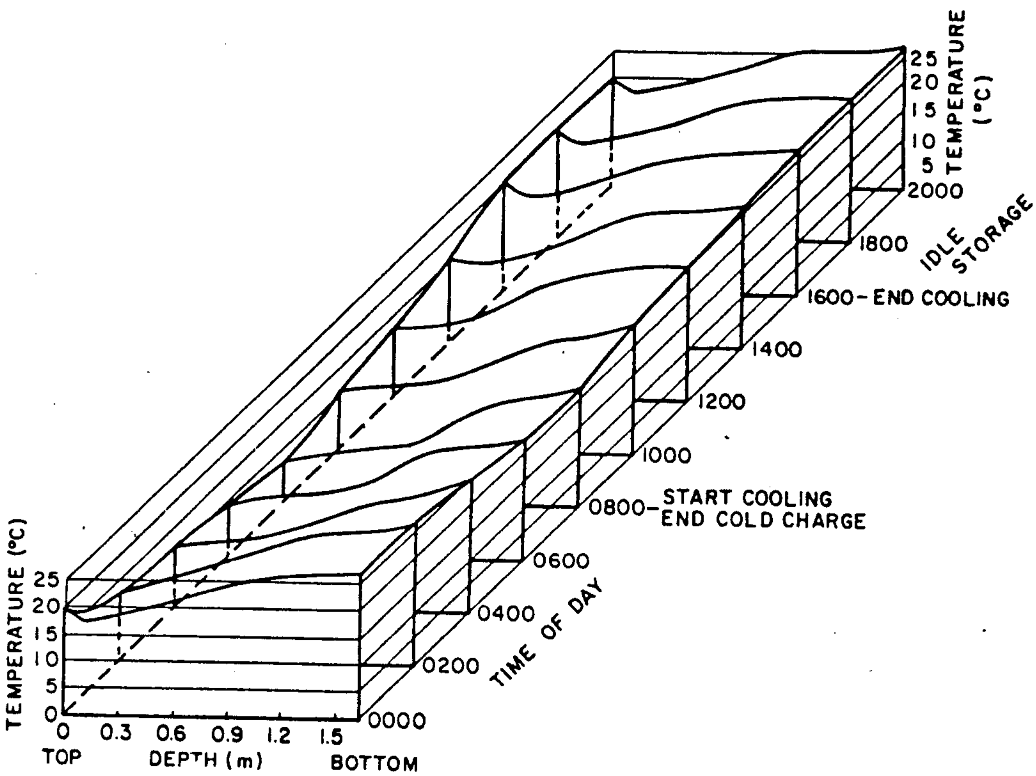

Figure 3.
Collector efficiency data from large sample of 10 minute data.

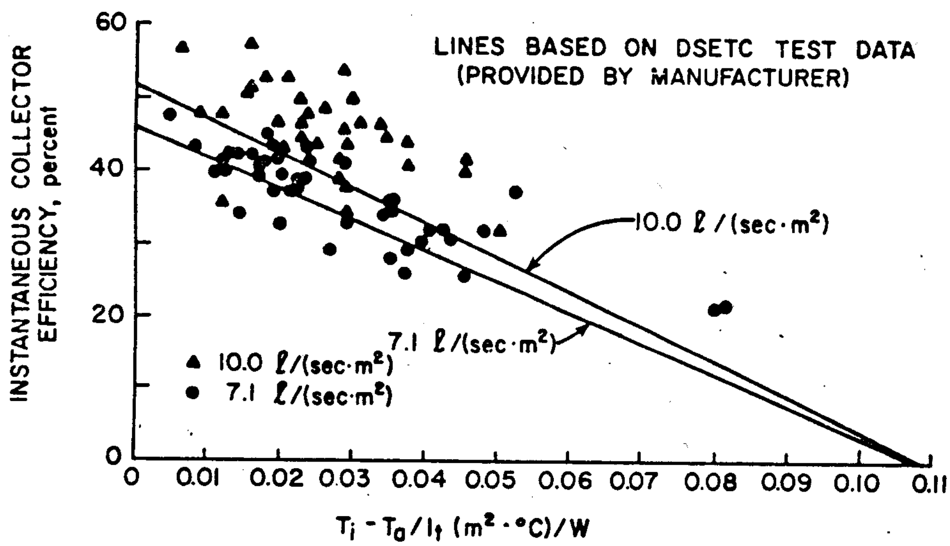

or a wind term:

$$\frac{q}{I_t} = F_R \tau\alpha = F_R U_L \ (T_i - T_a) - F_R U_W V \ (T_i - T_a)$$

(where wind velocity, V, is an additional operating condition to be measured) or a thermal capacitance term:

$$\frac{q}{I_t} = F_R \tau\alpha - F_R U_L \ (T_i - T_a) + C_i \frac{dT_i}{dt}$$

can be estimated. One can then select the form of model that is "best" for a given engineering purpose. Once the desired form of the governing equation(s) has been established for a component model one can perform further studies. For example degradation of the selective coating on a collector plate can be tracked by least square estimation of the radiation loss term, $F_R \sigma\varepsilon$, from data obtained during a number of successive months.

One useful way of representing overall system performance is shown in Figure 4. The monthly energy contributions by solar and auxiliary energy to the space cooling and domestic hot water loads are shown. Four different hydronic heating systems were tested during the time periods indicated. It can be seen that month to month variations in the loads affect performance about as strongly as modifications to the systems themselves. Thus it is essential to develop adequate models to compare the performance of different types of systems. Side by side performance monitoring is often not feasible but it is possible to verify models of these systems with sufficiently accurate data from relatively short monitoring periods. Different systems can then be compared by simulation using identical weather and load conditions.

Another form in which overall system performance can be concisely reported is illustrated in Figure 5. Here the cumulative energy transfers into and out of the system are presented according to the path or mechanism of energy flow. Note the 2% difference between energy collected and energy supplied or lost. Part of this difference is a "heat balance closure error" due to instrument errors. It is important at this level of performance monitoring that all energy flows be measured so that this heat balance closure error can be calculated. This is the only reliable way to verify that the transducers and data acquisition system have been functioning properly. More will be said on the subject of heat balances in the next section.

Types of Solar Heating and Cooling Systems Monitored

One of the four hydronic systems for which performance was reported in Figure 4 is depicted schematically in Figure 6. The first step in planning the instrumentation of such a system is the construction of an energy flow network. Such a network is shown in Figure 7. The system is then instrumented to measure all of the major energy flows and internal energy of all energy storage components. This makes it possible to perform a heat balance on each subsystem and on each component.

Figure 4.
Energy input/output diagram
for an entire cooling season.

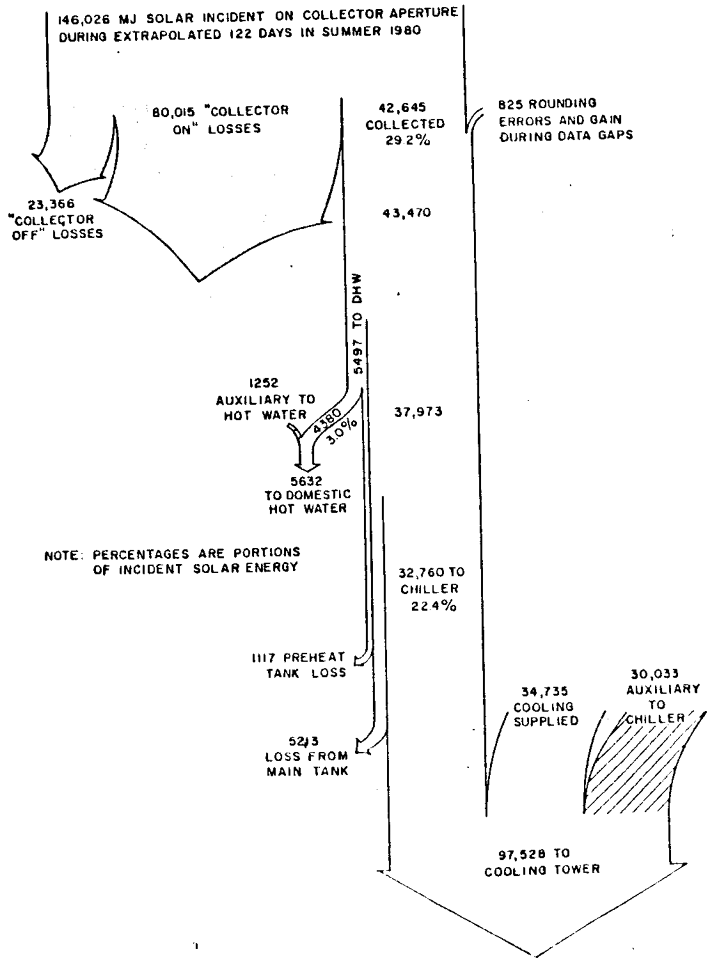

Figure 5.
Bar chart of monthly energy contributions.

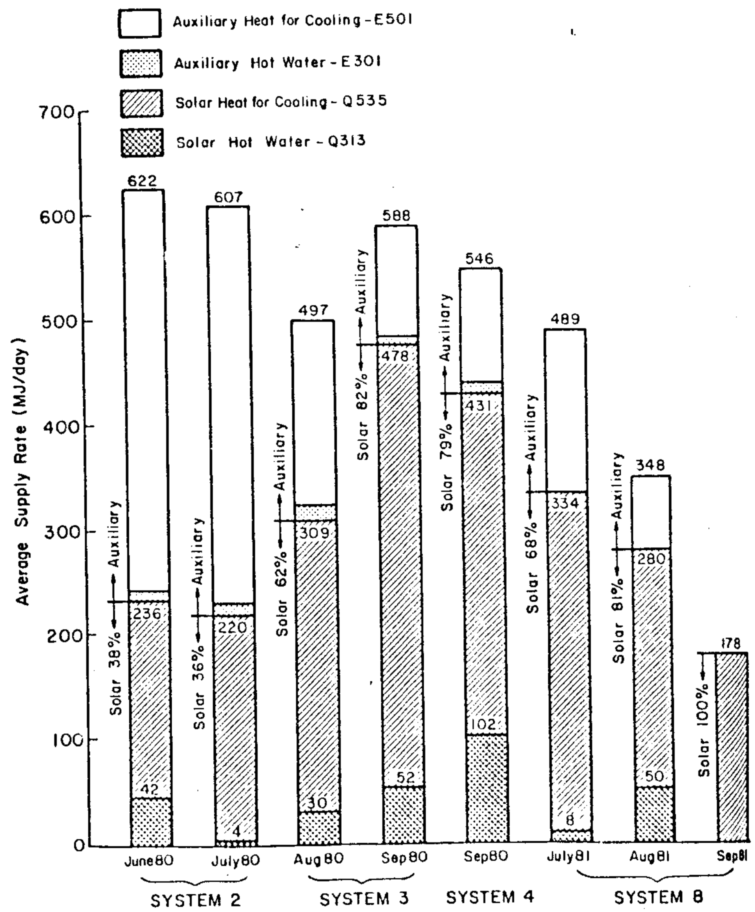

Figure 6.
Solar air heating system with parallel heat pump auxiliary which also employs off peak storage during the cooling season.

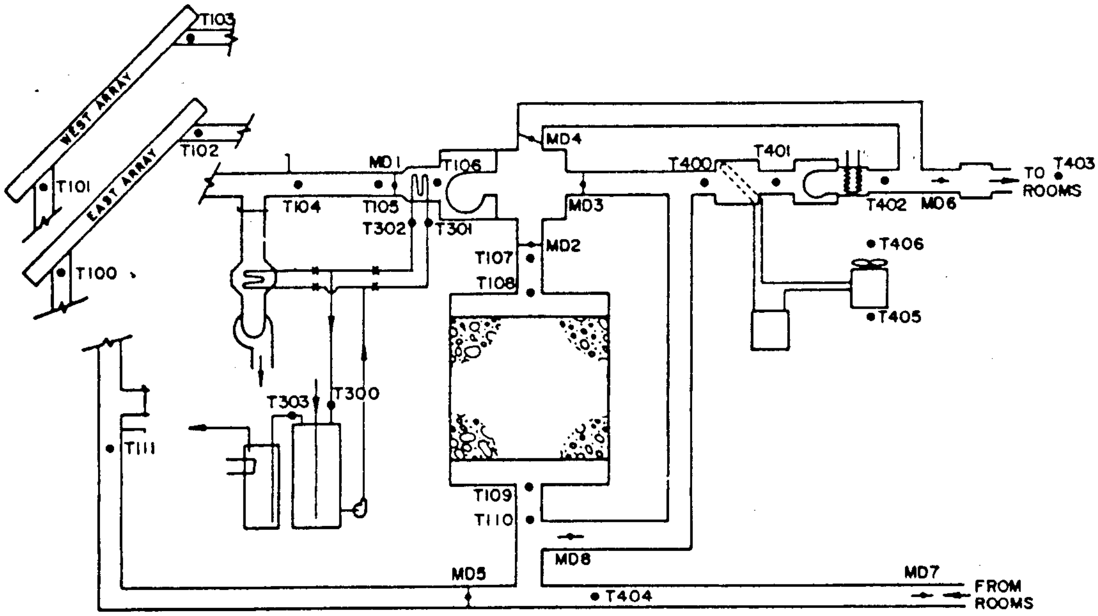

Figure 7.
Energy flow diagram of the system shown in Figure 6.

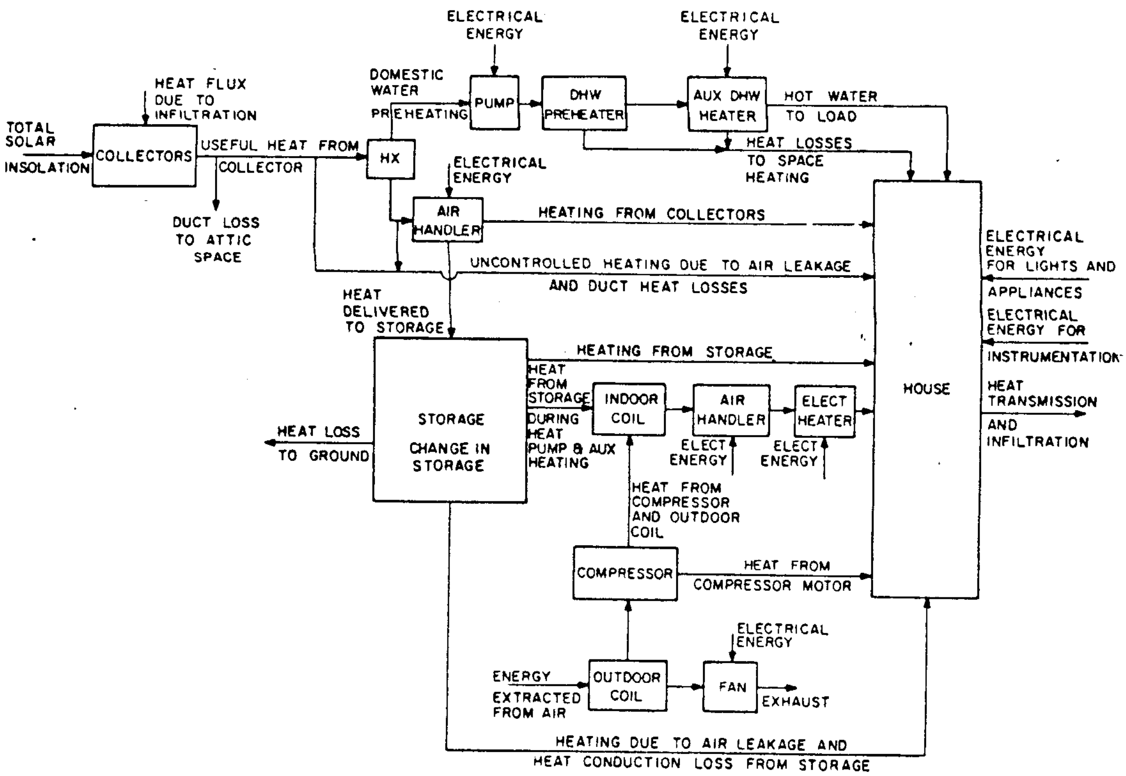

Determining all of the major energy flows in an air heating system, such as the one depicted in Figure 8 can be quite difficult. The reason for this is apparent from the corresponding energy flow network depicted in Figure 9. A number of the major energy flows are due to "air leakage" and "infiltration." Also shown are energy flows due to "duct losses" which are generally much larger than the corresponding pipe losses of hydronic systems. Some of these energy flows can be measured with reasonable accuracy. Some can be calculated based on other measurements. However some, such as the energy flow due to air leakage from storage, are very difficult even to estimate. Because air leakage compounds the problem of flow measurement in air systems a great deal of work has gone into air flow measurement at CSU. Some of the results of this work are reported later in the paper.

Energy Flow in Fluid Streams

Most of the measurements on these heating and cooling systems are ultimately used to compute energy flow rates associated with the continuous heating or cooling of fluids. Heat transfer rates of this sort are evaluated by an equation of the form

$$\dot{Q} = \Delta T \dot{m} c_p$$

where

ΔT = temperature difference

$\dot{m}$ = mass flow rate of the fluid

c_p = specific heat of the fluid.

The mass flow rate is usually evaluated by an equation of the form

$$\dot{m} = VA\rho$$

where

V = average velocity of the fluid

A = cross sectional area of the pipe or duct where fluid velocity is measured

ρ = fluid density

The quantity of heat transferred between two points in time, t_o and t_n, are evaluated by integration:

$$Q = \int_{t_o}^{t_n} \Delta T \, \dot{m} \, c_p \, dt.$$

Figure 8.
Solar hydronic heating and cooling system.

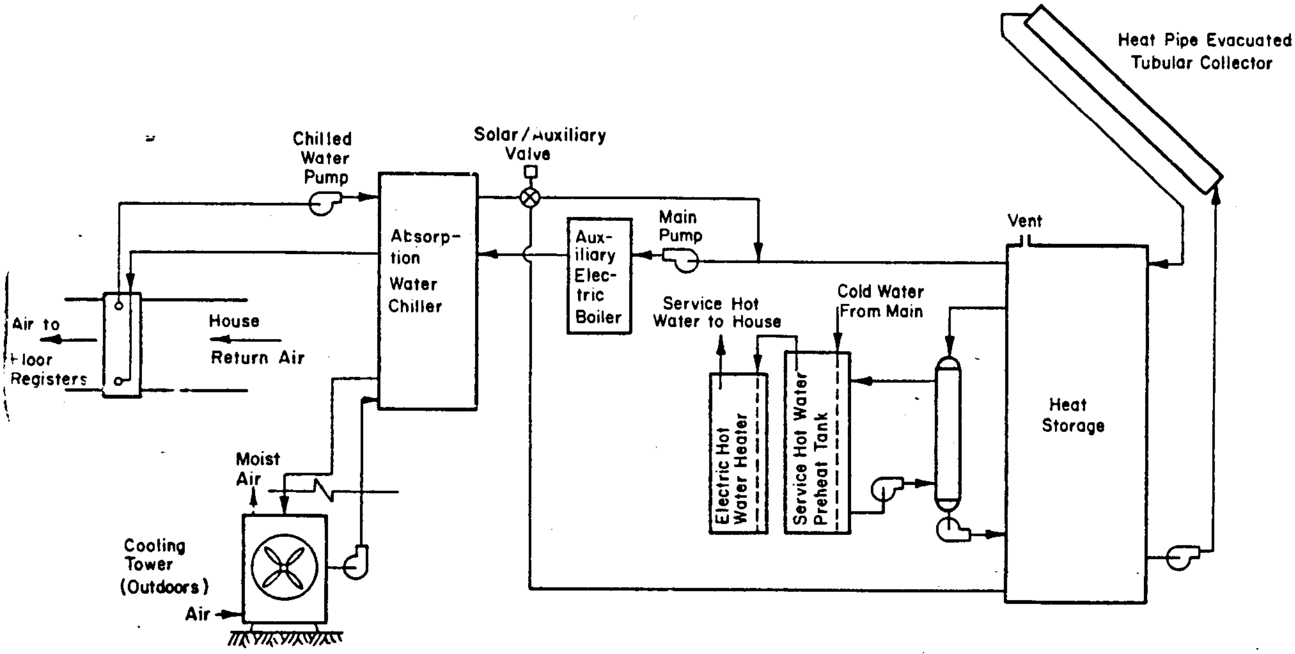

Figure 9.
Energy flow diagram of system shown in Figure 8 operating in the heating mode.

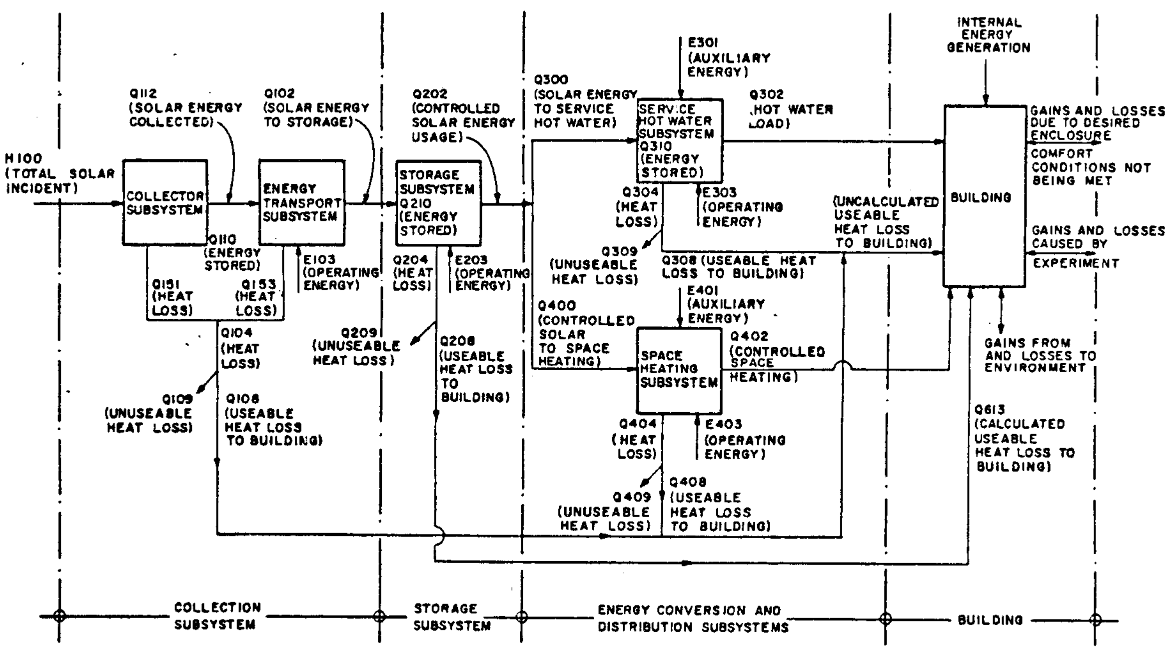

The integral is generally approximated by:

$$Q = \Delta T_o \dot{m}_o c_p \frac{\Delta t}{2} + \sum_{i=1}^{n-1} \Delta T_i \dot{m}_i c_p \Delta t + \Delta T_n \dot{m}_n c_p \frac{\Delta t}{2}$$

or by:

$$Q = \sum_{i=\phi}^{n} \left[\frac{\Delta T_i + \Delta T_{i+1}}{w} \int_{t_i}^{t_{i+1}} \dot{m} \, dt \; c_p \right]$$

where $\Delta t = t_{i+1} - t_i$ is the "<u>sampling interval</u>" (time between data logger "scans").

Sampling intervals of 1, 5, 10 and 15 minutes have been used at CSU.

The density, ρ, used to evaluate $\dot{m} = VA\rho$, is typically evaluated from established density-temperature functions for the aqueous solutions encountered in the hydronic systems. In air systems density is typically computed from a reference density corrected for measured barometric pressure, humidity and temperature. At any rate, the most common measurements in CSU's active heating and cooling systems are temperatures, temperature differences, and flows.

<u>Thermopiles for Measuring Temperature Differences</u>

Temperature differences encountered in the CSU hydronic systems were originally computed by taking the difference between separate thermocouple readings. However reference junction errors and limited data logger resolution resulted in errors that often exceeded .5 K. Consequently a 5 K measured temperature difference could easily be in error by more than 10%. Furthermore, over half of this error typically appeared as a relatively constant offset error. This resulted in systematic errors in calculated energy flows.

Temperature differences in the CSU air system on the other hand have been measured with thermopiles from the outset. Eight or more pairs of junctions are used in the fabrication of each thermopile. The junctions are distributed across the duct at each measuring station as shown in Figure 10 to obtain an average temperature difference when the air is not fully mixed. Temperature gradients can exist perpendicular to the flow in such cases. Large gradients are actually fairly common downstream of certain pieces of equipment such as the air-water heat exchanger.

Properly fabricated and installed thermopiles are inherently zero offset devices. The scale factor error can be taken to be the ASTM scale factor error (i.e. the "percent of reading" error component). Thus type T thermopiles fabricated from "premium" or "special limits" grade wire are accurate to within ± .4% of reading. This figure has been verified in calibration tests at CSU and SERI. The data logger will contribute a small *offset error that is usually less than .05 K. For example, a 5 microvolt* offset error results in a .01 K offset error when temperature difference is measured by a 9 pair, type T thermopile.

Figure 10.
Location of six pairs of junctions at two duct cross sections for measuring average temperature difference in an air heating system by means of a thermopile.

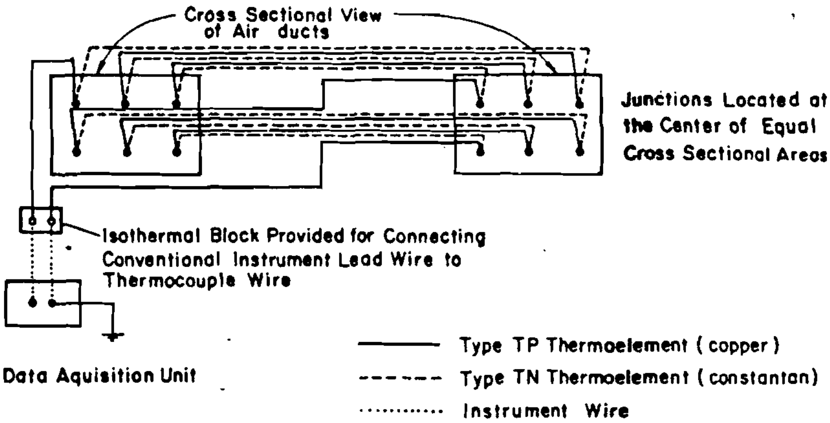

A practice of measuring temperature differences in a complete circuit around each fluid loop (i.e. between every contiguous pair of measuring stations) has proven useful. Two such circuits are shown in Figure 11 where it is seen that even the small temperature changes associated with heat loss from duct runs are measured. The temperature differences measured around the loop are summed at every scan. The sum is compared to an error limit, e.g. ± (.1 K + 1% of the difference between the highest and lowest temperatures in the loop). The results of this procedure give added confidence in thermopile accuracy as well as a means of detecting thermopile, probe, or leadwire faults.

Figure 11.
Location of temperature measuring stations in an air heating system. Note the practice of linking each successive pair of measuring stations with a thermopile in order to directly measure all temperature differences around the loop.

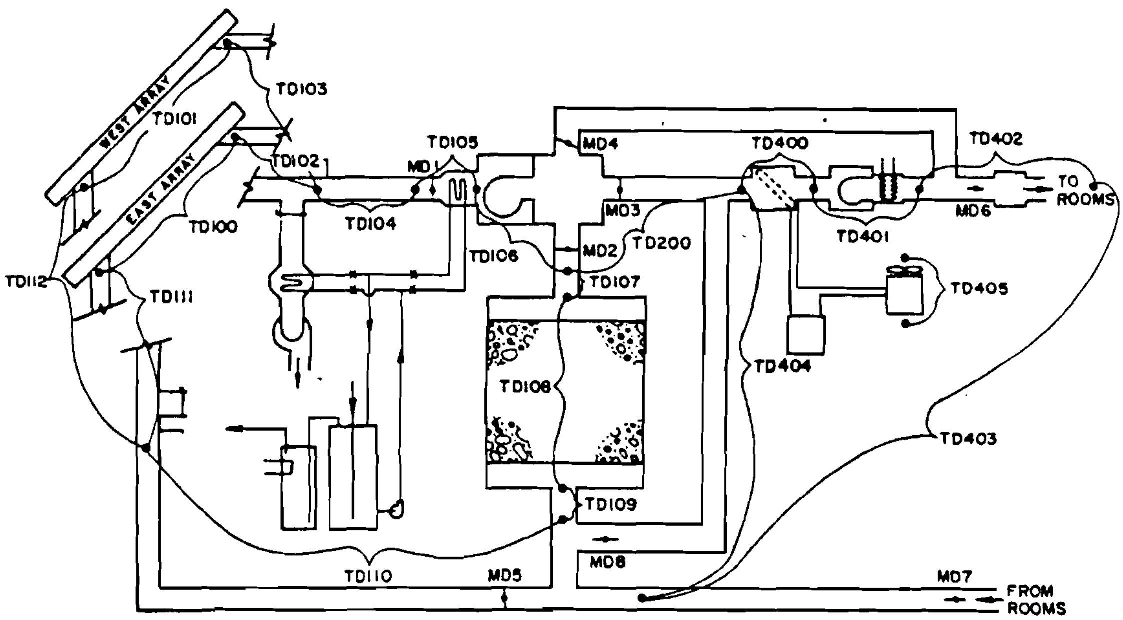

Figure 12.
A prototype loop of three thermopiles and three probes. Most applications require more than three measuring stations and greater lengths of thermopile cabling between probes.

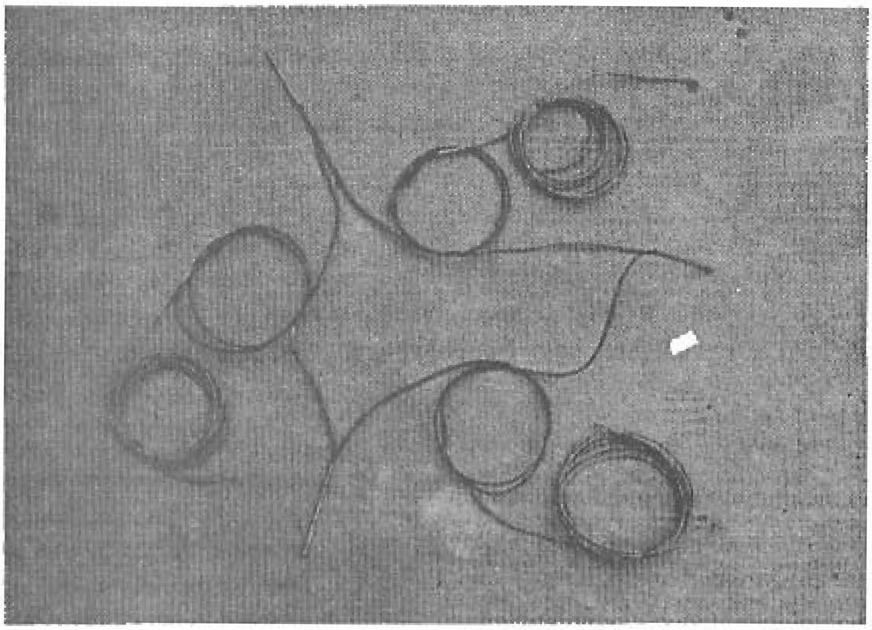

Figure 13.
Temperature measuring station at a collector header inlet with three separate probes. One probe is provided for each of the three thermopiles that terminate at this station.

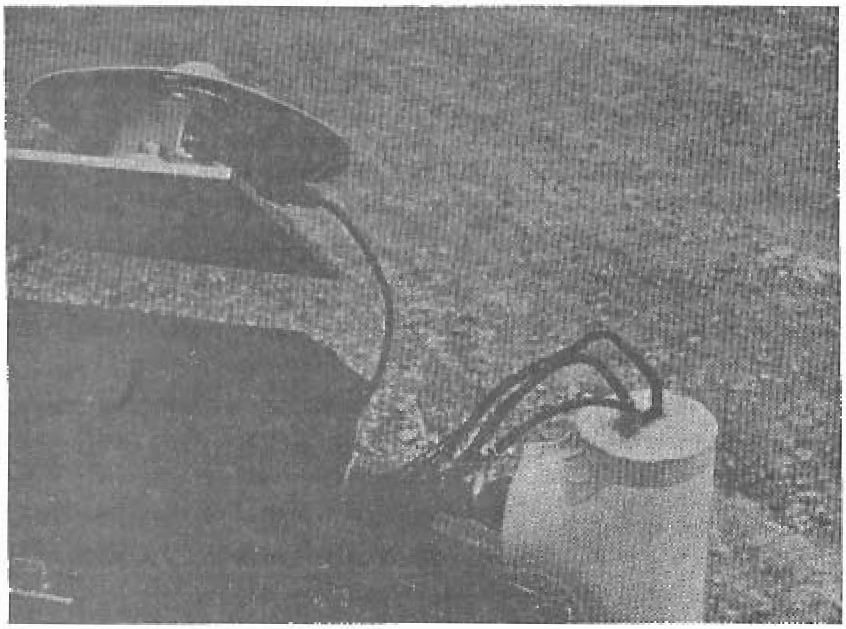

Figure 14.
Temperature measuring station with thermopile end removed from probe to show liberal use of thermal grease to reduce probe error.

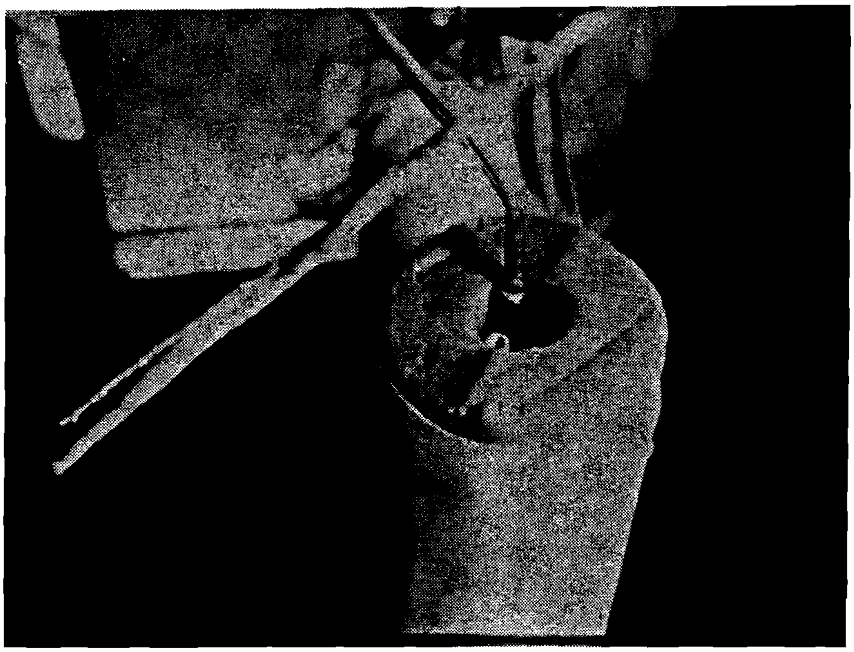

Converting Thermopile Voltage to Temperature

Thermopiles are somewhat non-linear. Over the range of temperatures encountered in low temperature solar applications most types of thermopile have a positive temperature coefficient, i.e. their sensitivity increases with temperature. In any case it is always necessary to measure the temperature at one end of the thermopile to perform the voltage to temperature conversion. However, because the thermopile nonlinearity is weak, only a small fraction of the error in this "reference temperature" measurement is propagated to the resulting temperature difference.

Three thermopile conversion algorithms are in common use [3]: the first uses the standard form of the thermocouple curve [4], the second uses a table of thermopile coefficients with linear interpolation, and the third uses a bivarite function, $S(\Delta e, T_{ref})$, fit to the table of thermopile coefficients. The first method was employed at C.S.U. for a time [5] but discontinued in favor of the less computationally burdensome third method.

The third method is simpler in part because it is usually unnecessary for the thermopile conversion function to be fitted over the entire range of the standard thermocouple curve. A lower order polynomial may therefore be used. Coefficients in the thermopile sensitivity function depend on the *thermocouple type as well as the temperature range. Over the temperature* range $-35^{o}C < T_{ref} < 115^{o}C$ and $-100K < \Delta T < +100K$ the conversion functions may be approximated by:

$$S = 25.89 - .05749\ T_{ref} - .7447\Delta e + .0001635\ T_{ref}^2 + .005557\ T_{ref}\ \Delta e + .4654\ \Delta e^2$$
$$- .4475\text{x}10^{-6}\ T_{ref}^3 - .00002107 T_{ref}^2\ \Delta e - .0003793\ T_{ref}\ \Delta e^2 - .002188\ \Delta e^3$$

for type T within .08% rms, +.47% maximum and -.07% minimum error, and

$$S = 19.86 - .02447\ T_{ref} - .2446\Delta e + .0001044\ T_{ref}^2 + .002155\ T_{ref}\Delta e + .01341\ \Delta e^2$$
$$- .1554 \times 10^{-5}\ T_{ref}^3 - .00004093\ T_{ref}^2\ \Delta e - .0005038\ T_{ref}\ \Delta e^2 - .002351\ \Delta e^3$$

for type J within .04% rms, +.25% maximum and -.08% minimum error. Using the appropriate expression for S, the temperature difference in Kelvins is calculated by $\Delta T = S\Delta e$ where Δe is the measured thermopile voltage in millivolts divided by the number of junction pairs.

Two practices have been used at CSU to obtain the "reference temperature" measurements needed for thermopile conversion. Both use thermocouples and work equally well. The first is to simply insert an extra thermocouple in the probe along with the thermopile leads. The second involves splicing into the thermopile a pair of thermocouple leads so that the data logger can treat one of the thermopile junctions as if it were a separate thermocouple. This method will only work if certain grounding and data logger requirements are met as discussed in [5].

Air Flow Measurement

The essentially constant volumetric flow rate property of most residential HVAC blowers has been used to advantage in measuring flow rates in the CSU solar air heating system. The scheme involves determining long term average flow rates for each mode of operation and duct location of interest. Calibrated, low cost Pitot rakes such as the one shown in Figure 15 are used as the primary measuring elements. Airflow measuring stations W108 and W109 are shown in Figure 16 with the pitot rake module for station W109 partially removed. A large number of flow stations are needed because air leaks result in large differences in mass flow rate at different points about a "closed loop." The locations of the thirteen measuring stations used to monitor the parallel heat pump system are shown in Figure 17.

The Pitot rakes produce very low differential pressures (around .1 millibar) at the air velocities being measured (around 3 m/s). The cost of a secondary measuring element (differential pressure transducer) with adequate accuracy specifications is therefore quite high (around $3000). Consequently a measuring system has been developed in which a single transducer is used to monitor a number of air flow stations. We call this "pneumatic time-division multiplexing."

Figure 18 shows the differential pressure transducer (lower right) and its associated electronics (top). The back of the panel to which pneumatic tubes from the Pitot rake stations connect is visible (center); the 2-gang 12-position

Figure 15.
Pitot rake module showing the eight total pressure taps and manifold (copper), two static taps (aluminum), and the honeycomb air straightener (dark area). The module measures air flow toward the viewer therefore the total pressure taps point away from the viewer (upstream).

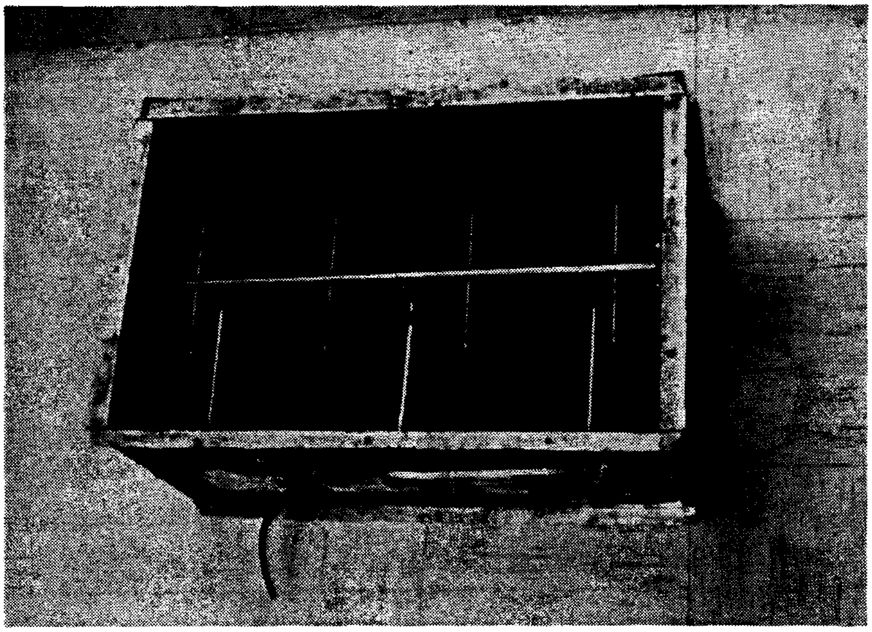

Figure 16.
Air flow measuring stations in the duct leading to the lower rock bed plenum. The station from which the Pitot rake module has been partly removed measures flow when storage is being charged (flow to the left). The other station measures flow during discharge (flow to the right).

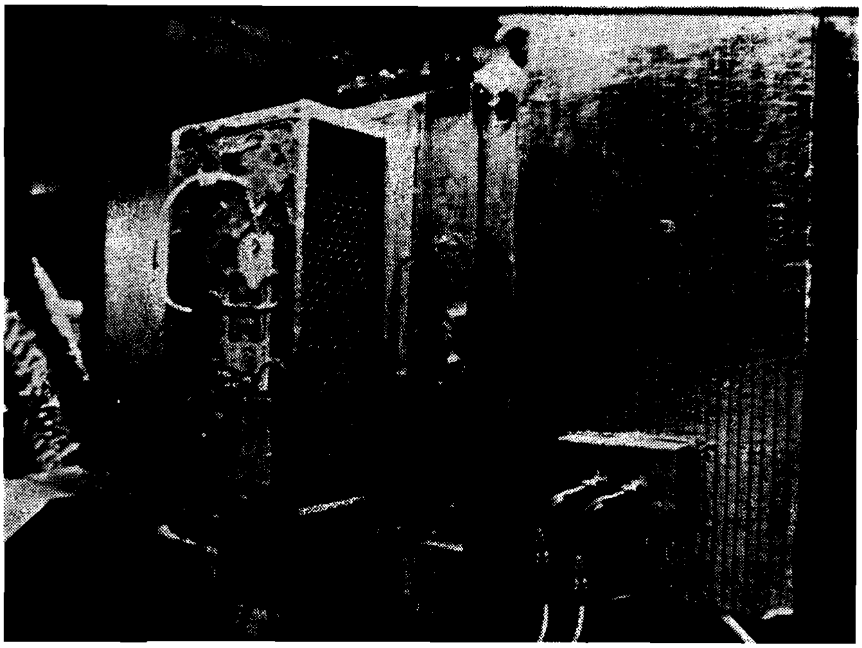

Figure 17.
Location of air flow measuring stations in the solar air heating system with parallel heat pump and off-peak cooling capability. Note the location of stations at both collector inlets and outlets to determine leakage rates.

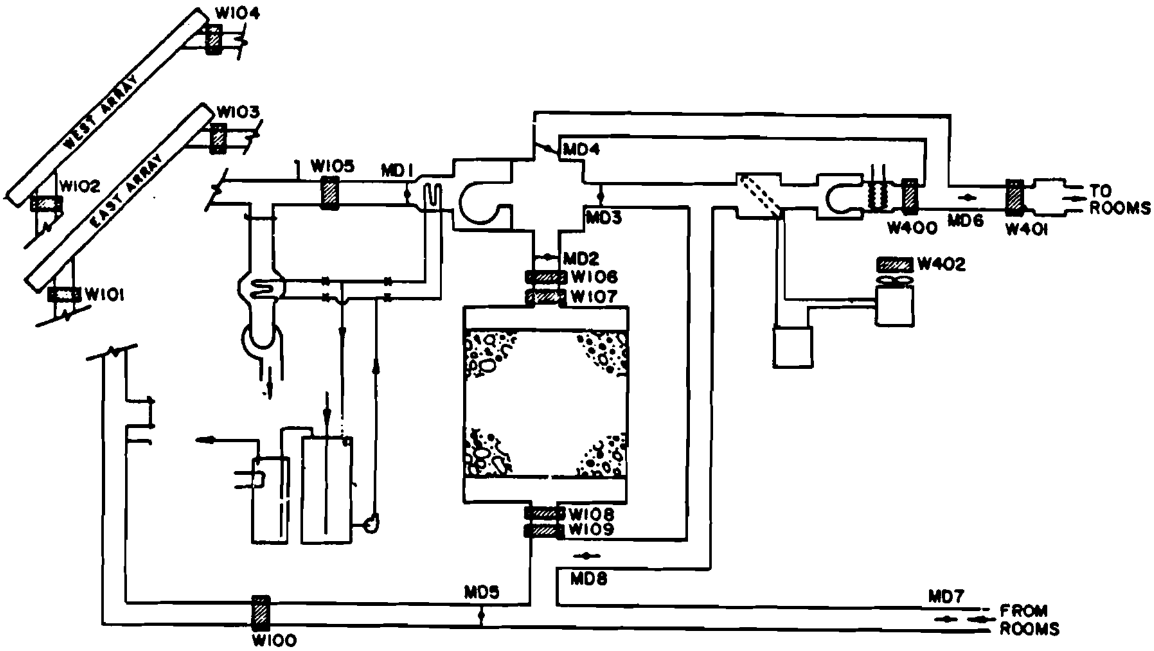

Figure 18.
Pneumatic multiplexer and differential pressure transducer for sampling the dynamic heads developed by up to 11 pitot rake air flow measuring stations.

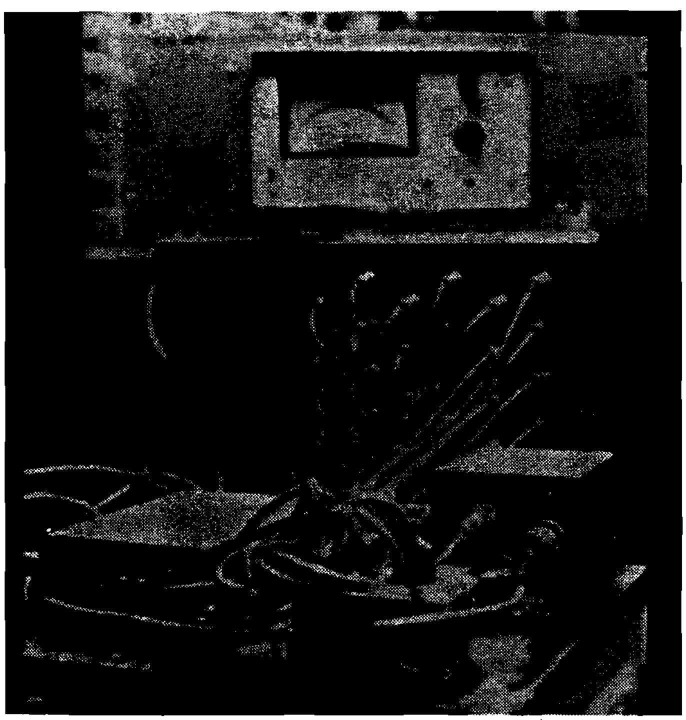

Figure 19.
Block diagram of the air flow measuring system and its relation to the data logger and the monitored system.

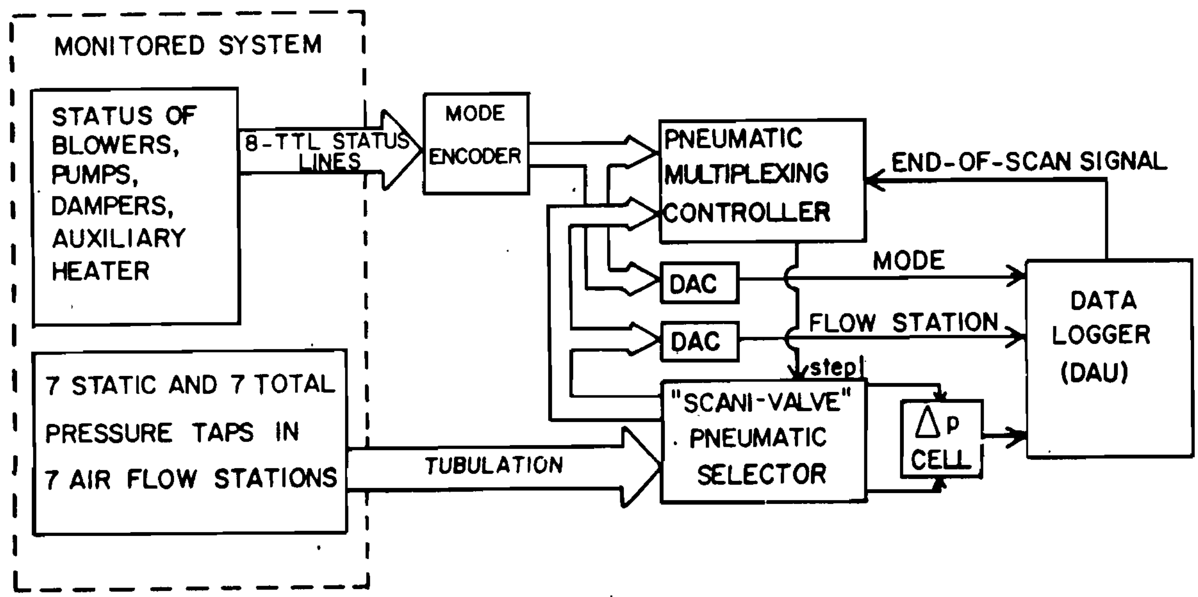

valve (pneumatic switch) to which the internal tubes connect, is hidden. The valve position controller appears to the lower left. A heater maintains the pressure transducer at 60°C to reduce fluctuations in zero offset. With this multiplexing scheme only one station can be monitored at each scan (scans occur every 10 minutes). The resulting sampling rate is nevertheless sufficient for obtaining long term average flow rates and even to detect changes in the average flow rates that occur as frequently as every few days.

A block diagram of the air flow measuring system is shown in Figure 19. Two such systems are in use with a total capacity of 22 air flow measuring stations. The purpose of the pneumatic multiplexing controller is to determine the operating mode of the heating system and to sequentially select air flow stations that are active in that mode.

The controller operates as follows. A pneumatic switch, which connects the differential pressure transducer pneumatically to one of twelve pneumatic circuits is stepped through its twelve positions sequentially. Up to eleven of these positions may connect to Pitot rakes at various locations in the system while the twelvth is connected to a pneumatic short circuit for measuring the zero offset of the differential pressure transducer. Stepping commences after each scan. At each step the mode and switch position are input to a truth table whose output is True if the air monitor corresponding to the switch position is active in the indicated mode and False if it is not. On False another step is initiated; on True stepping stops. Eventually the differential pressure transducer is connected pneumatically to an active air monitor or to the pneumatic sort. A scan occurs, the differential pressure reading is secured, and the whole process is repeated. A schematic of the controller is shown in Figure 20.

The volumetric flow rate corresponding to the measured differential pressure is calculated first at local conditions of temperature and pressure and then at blower conditions. The variables used in these calculations are defined below:

$\dot{V}_\ell$, $\dot{V}_B$	Volumetric flow rate: at local (air monitor) density (ℓ), and at blower density (B)
A_ℓ	Duct cross-sectional area at monitor
C_ℓ	Air monitor pitot coefficient (determined by calibration)
V_ℓ	Flow velocity
Δp	Dynamic pressure
$\rho_o, \rho_\ell, \rho_B$	Air density: standard, at the monitor, and at the blower
p_o, p_ℓ, p_B	Static pressure: standard, at the monitor, and at the blower
T_o, T_ℓ, T_B	Temperature: standard, at the monitor, and at the blower

The local volumetric flow rate is given by:

$$\dot{V}_\ell = C_\ell A_\ell V_\ell = C_\ell A_\ell \sqrt{\frac{2\Delta p}{\rho_\ell}} = C_\ell A_\ell \sqrt{2\Delta p \frac{p_o T_\ell}{\rho_0 T_0 p_\ell}}$$

The local pressure, p , is taken to the the atmospheric pressure within the building envelope uncorrected for pressure distribution within the ducts. Such a correction is less than two parts per thousand in most air systems and is thus unimportant. In practice, the product, C A is determined by calibration of individual air monitors, as discussed in the next section.

The local volumetric flow rate, $\dot{V}$, is then converted to blower equivalent air density and the negligible pressure correction eliminated giving:

$$\dot{V}_B = \frac{\rho_\ell}{\rho_B} \dot{V}_\ell = \frac{p_\ell}{p_B} \frac{T_B}{T_\ell} \dot{V}_\ell \doteq \frac{T_B}{T_\ell} \dot{V}_\ell$$

As pointed out in [3] there is theoretical justification for expressing all volumetric flow rates at blower conditions. In a fluid circuit with a constant volume motor-blower, constant temperature along the flow path and stable leakage, volumetric flow rates would be expected to be constant everywhere. The introduction of temperature changes along the flow path results in expansion (or contraction) of the air as it is heated (or cooled) locally thus increasing (or decreasing) the volumetric flow rate at any given point in the loop. Experimental results confirm that $\dot{V}_B$ has a tighter distribution, and thus smaller standard deviation than $\dot{V}_\ell$.

Figure 20. (below)
Schematic of the programmable pneumatic multiplexing controller.

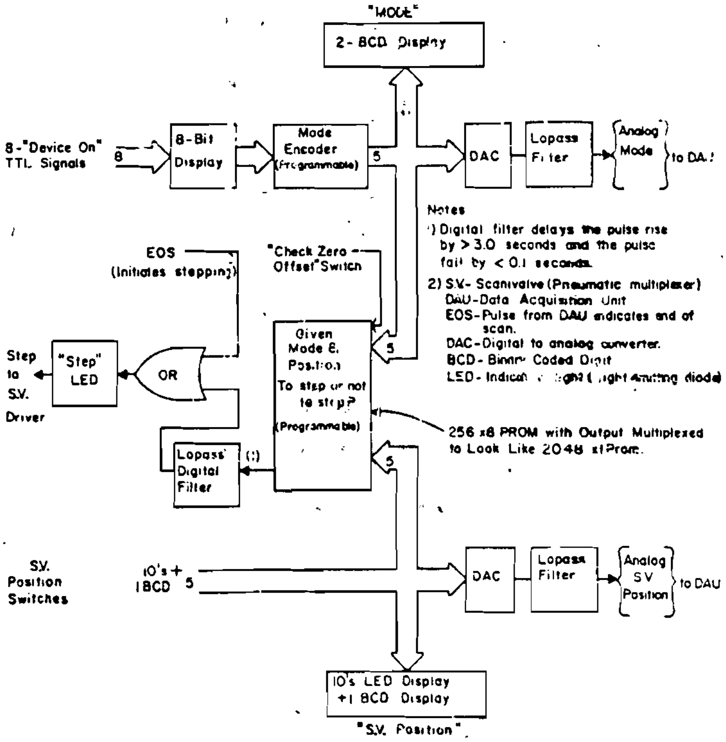

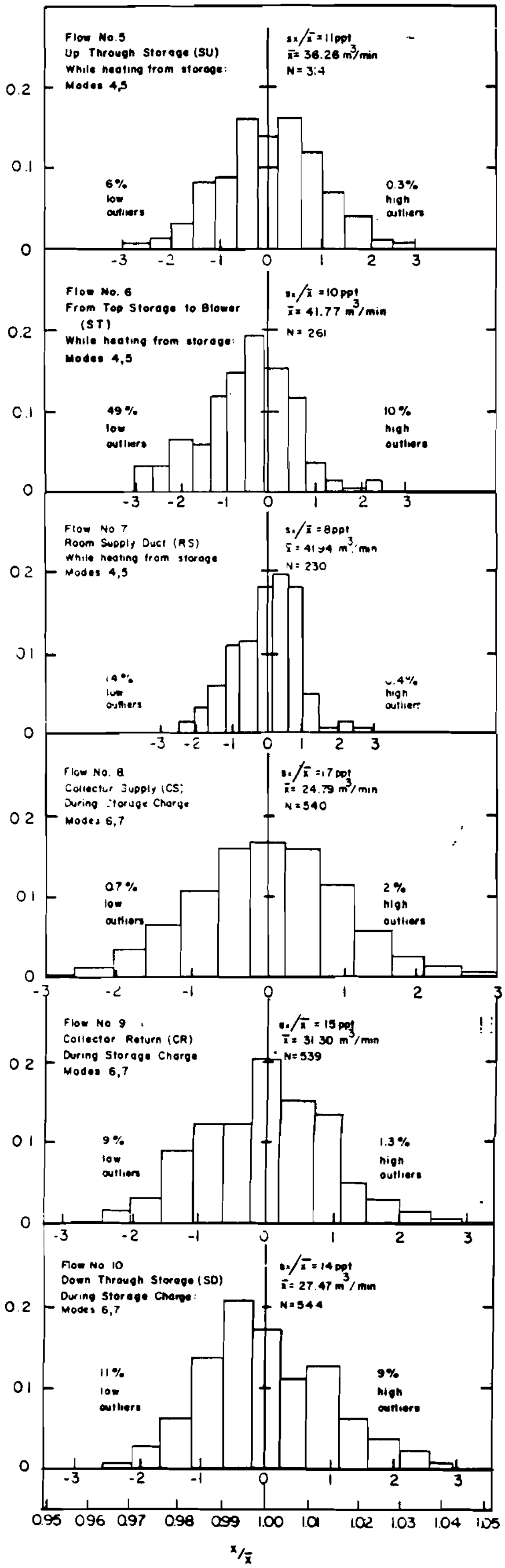

Figure 21. (left)
Airflow statistics from CSU Solar House 2. Two different operating modes are represented with flow measurements taken at three different locations for each mode. The random variable, x, is volumetric flowrate at blower conditions, designated $\dot{V}_B$ in the text. The main abscissa scale gives x normalized to the sample mean, $x/\bar{x}$. The abscissa scale below each relative frequency histogram gives deviation from the sample mean normalized to the standad deviation of the sample, $(x - \bar{x})/s_x$.

Figure 21 is representative of the statistical analysis applied to all of the flow data. The sample variance for the 3σ outlier rejection criterion is based on the standard deviation of the finally accepted sample and must therefore be solved iteratively in multiple pass data processing. The data are generally processed in two week samples in order to test for changes in the sample mean and variance.

Heat rates must always be calculated using the flow rate values which are valid at the time of the heat rate measurements. This is a disadvantage because the results of real-time data reduction must be corrected when a change in any of the rates is detected. Fortunately the averages have generally remained constant except for intentional adjustments. Advantages of this scheme are that instrument malfunctions are quickly detected (by the ratio of samples accepted to samples rejected or by changes in the sample mean or variance) and transient flow readings, which can potentially introduce large heat balance errors, are rejected according to a formal, reliable procedure. The scheme provides good accuracy (within ± 2% of the true steady state average at velocities of around 3 m/s) at relatively low cost when the number of air flow stations is more than about five.

Calibration of Air Flowmeters

Basic plans and procedures for the calibration rig appear in ASHRAE [6], ASHRAE [7] and NBS [8]. However these documents are somewhat incomplete. The equipment and procedures that were found to work well at CSU are therefore presented below.

The basic nozzle apparatus is shown schematically in Figure 22 and pictorally in Figure 23. Construction details are shown in Figure 24. The box is fabricated of plywood with continuous corner blocks of fir or pine which are screwed and glued to ensure air tightness. Wooden flanges are installed to accept the inlet adapter (this is an external flange) the diffuser baffles, and nozzle baffle, and an access cover. Closed cell foam gaskets are carefully bonded to the inlet, nozzle, and access cover flange faces. To minimize leakage, holes for the inlet adapter fasteners are drilled outside of the gasket; nozzle baffle holes are drilled through the gasket.

The diffuser baffles are perforated plates with approximately 40% free area, uniformly distributed. Commercially available perforated screen with about 0.5 cm holes is satisfactory except when a very small nozzle is used; the diffuser perforations should be less than 1/5 the nozzle diameter. Moderate leakage into the nozzle outlet plenum from the outside is permissible. However, leakage between the nozzle inlet plenum and the outside, or between the inlet plenum and the outlet plenum, must be minimized. The leakage rates were measured using the apparatus shown in Figure 24. The leak test procedure follows.

With a solid adapter plate covering the inlet flange, a vacuum cleaner is used to draw the plenum gauge pressure down to what will be encountered during operation at full flow. Leakage, as inferred from Δp across the orifice, was less than 0.1% of the full flow.

Figure 22.
Schematic of air flow calibration rig employing a 6 inch diameter ASME standard nozzle.

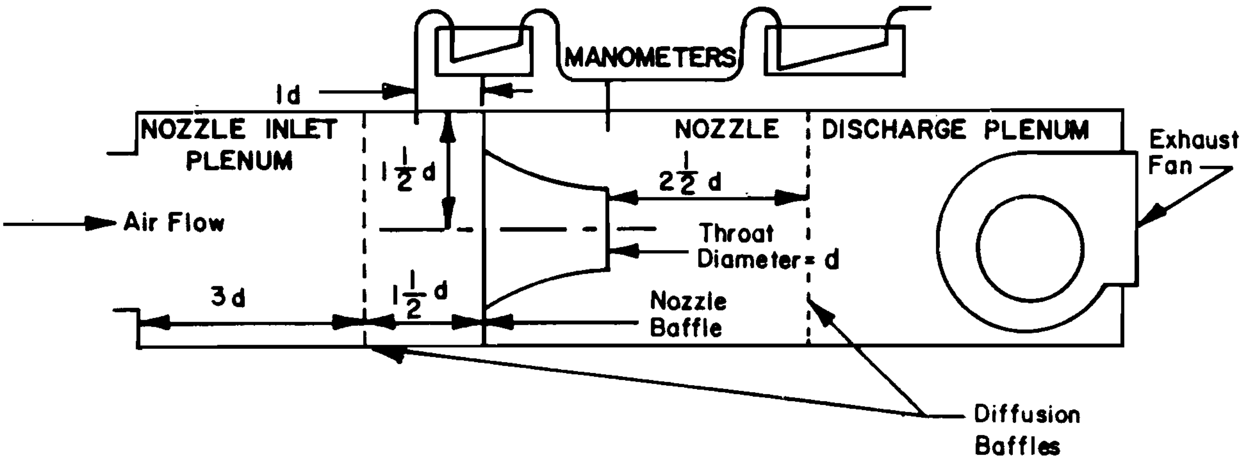

Figure 23.
Photograph of the air flow calibration rig.

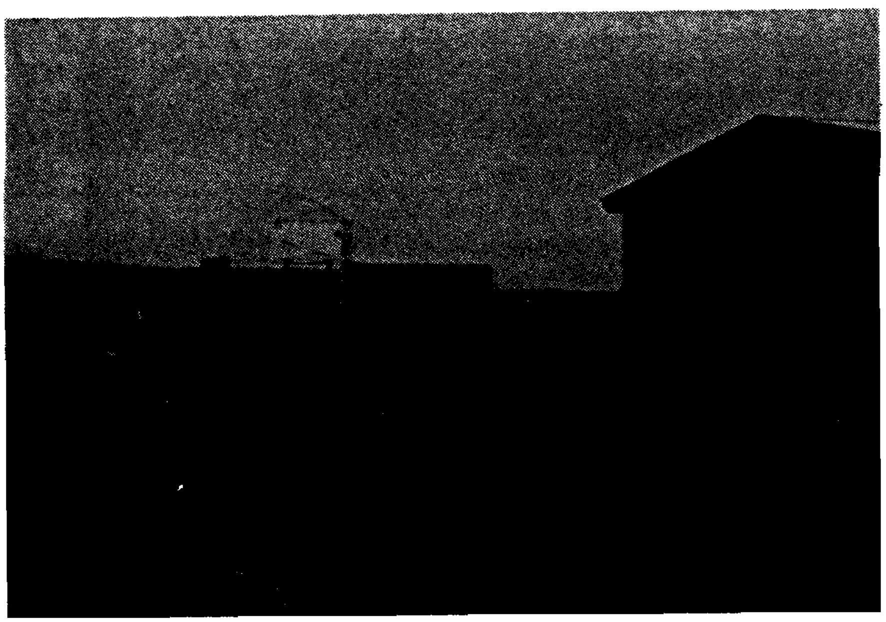

Figure 24.
Apparatus for checking leakage into the nozzle inlet plenum.

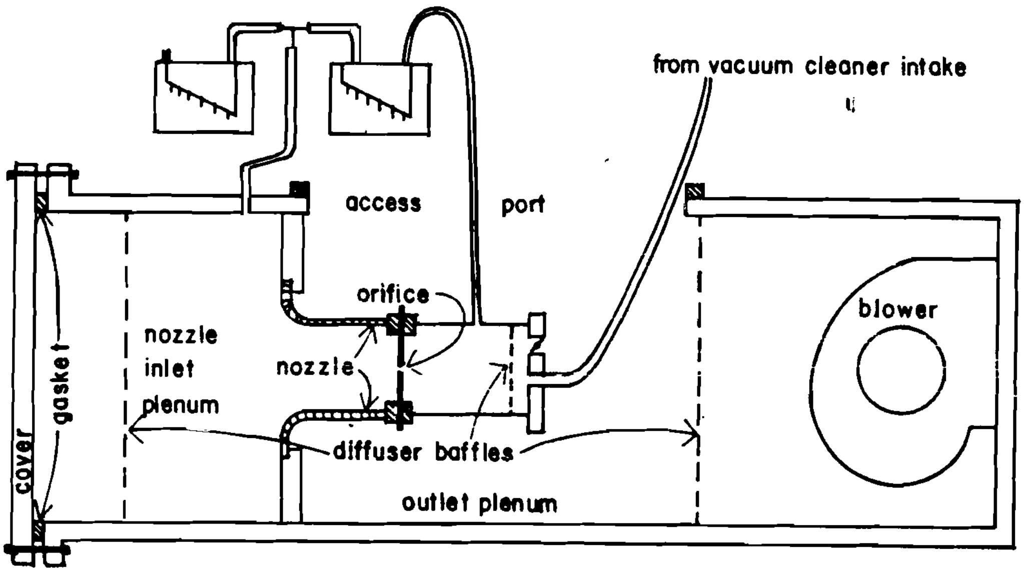

Figure 25.
Acrylic nozzle turned to ASME long radius nozzle standards (left) and a micromanometer (right) for measuring nozzle pressure drop.

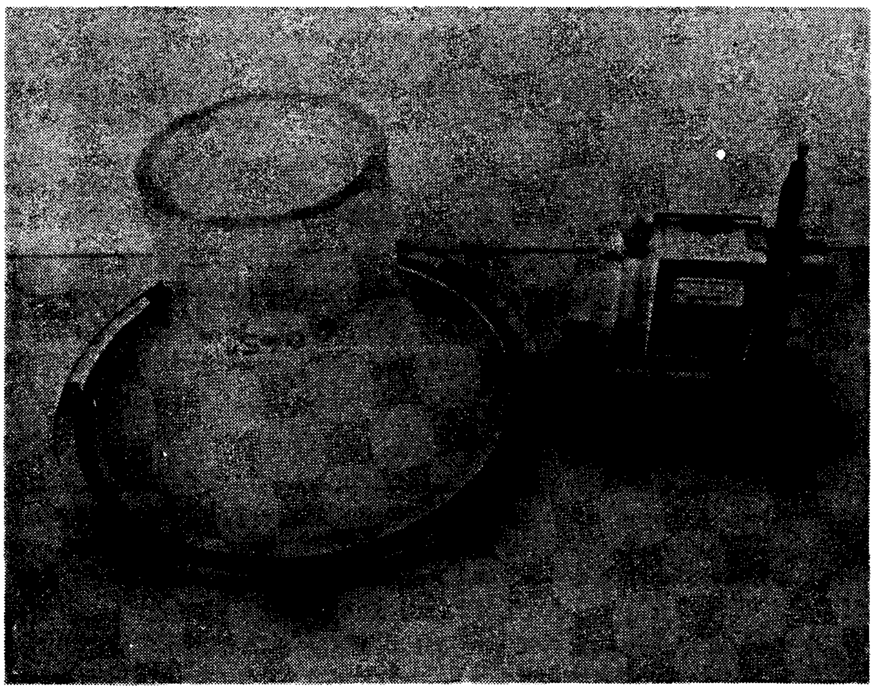

When selecting a nozzle and blower/motor set, the range of volumetric flow rates and resulting nozzle pressure drops must be considered. The nozzle pressure drop at a maximum throat velocity of 35 m/s (115 fps) is 700 N/m^2 (2.8 inches water) at standard air conditions. (The diffuser baffles add only about 3% to the nozzle pressure drop.) This pressure drop is considerably larger than that encountered in the CSU solar air heating system, so a correspondingly larger motor was required to drive the calibration rig. Flow rate modulation was provided by changing drive ratios and by an adjustable damper at the blower.

The nozzle shown in Figure 25 was turned in the CSU Engineering Research Shop. The nozzle's throat diameter was determined precisely before installation in the nozzle apparatus by measuring the inside diameter at four locations in the throat to an accuracy of 0.05%. The four measurements should agree to within 0.2% and their average used to calculate the cross-sectional area of the throat. Nozzles manufactured to ASME long radius nozzle specifications are available in eight sizes between 4 and 22 cm (50% increments) from Air Filter Testing Laboratories, 1912 Production Dr., Louisville, KY 40299. Smaller nozzles are available from Cox Instrument, 15300 Fullerton, Detroit, MI 48227.

A good square edge static pressure tap which mounts flush with the plywood wall has been fabricated at low cost from a flat heat carriage bolt as shown in Figure 26. Taps are installed 0.5d upstream and 1.0d downstream of the nozzle baffle. It is important that no leaks exist in the static tap tubulations and that the manometer have a precision of 0.05 mm water column or better. A hook gauge or "micro-manometer," as shown in Figure 25, is required.

The calibration rig has been operated in a closed room so that inlet air is drawn directly from room ambient through a bell mouth opening leading into the test meter duct section, the nozzle, and finally, the blower. Blower exhaust air is discharged back into the room. It is simplest to measure barometric pressure in the room and add to it the static gauge pressure (a negative gauge pressure) measured in the nozzle outlet plenum. Air temperature and relative humidity (needed in addition to barometric pressure to calculate air density) are also measured at room ambient conditions thus eliminating the need for duct probes.

Liquid Flow Measurement

Orifice meters and differential pressure transducers were used for a time to measure flow rates in Solar House 1. However zero offset drift resulted in large errors. Industrial grade turbine meters have been used since then. With periodic individual calibration these meters provide good accuracy ($\pm$1%) at reasonable cost.

The turbine meters were originally calibrated against a mass standard as shown in Figure 27. The procedure follows:

Begin with the catch bucket (empty) and a standard mass, m_s, on one side of the balance and an excess of mass on the other side. Start pumping the fluid at a steady rate through the test meter and into the catch bucket. At the instant the balance crosses zero start integrating the meter's output.

Remove the standard mass from the catch bucket side of the scale; the mass on the other side is unchanged so it will again be in excess. When a mass of liquid equal to m_s has passed into the bucket, the balance will again cross zero. At the instant the balance crosses zero stop integrating

For a volumetric flowmeter the meter calibration is given by:

$$k = m_s/\rho V_{indicated}$$

where density, ρ, is measured or inferred from the temperature of the fluid, and $V_{indicated}$ is the cumulative volume indicated by the test meter.

Some potential sources of error which are eliminated by this procedure are:

1. volume measurement error: a mass standard is not affected by temperature of mechanical stress;

2. weighing scale nonlinearity: the scale is in the same position (the zero crossing point) at both the start and the finish of the run;

3. variation in fluid holdup volume: the volume of fluid held up in the pipes remains constant;

Figure 26.
Cheap square edge static pressure tap fabricated from flat head carriage bolt.

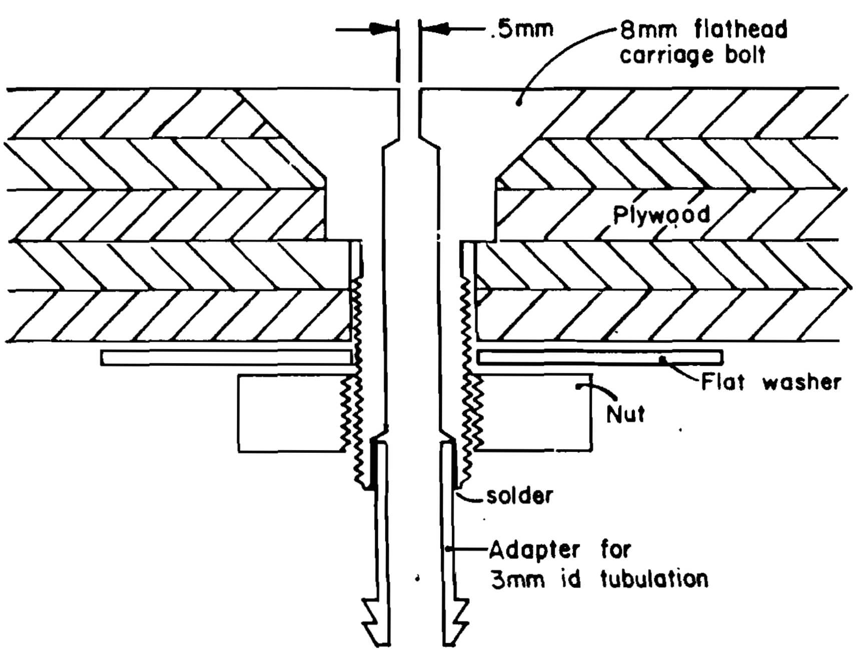

Figure 27.
Mass balance calibration rig for liquid flow meters.

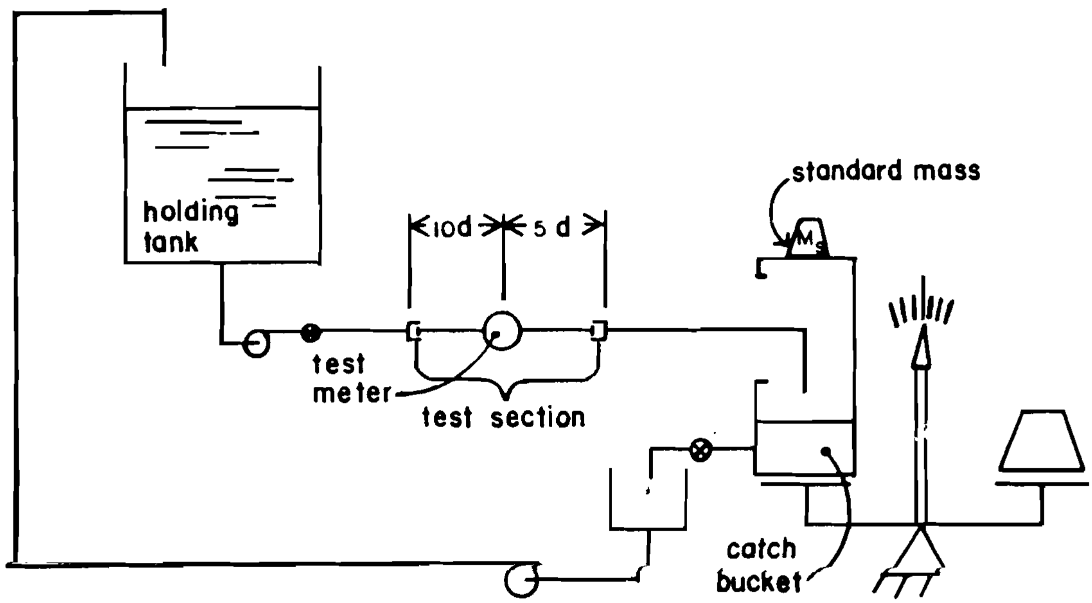

Figure 28.
Venturi meter and manometer used for in-situ calibration of turbine meters.

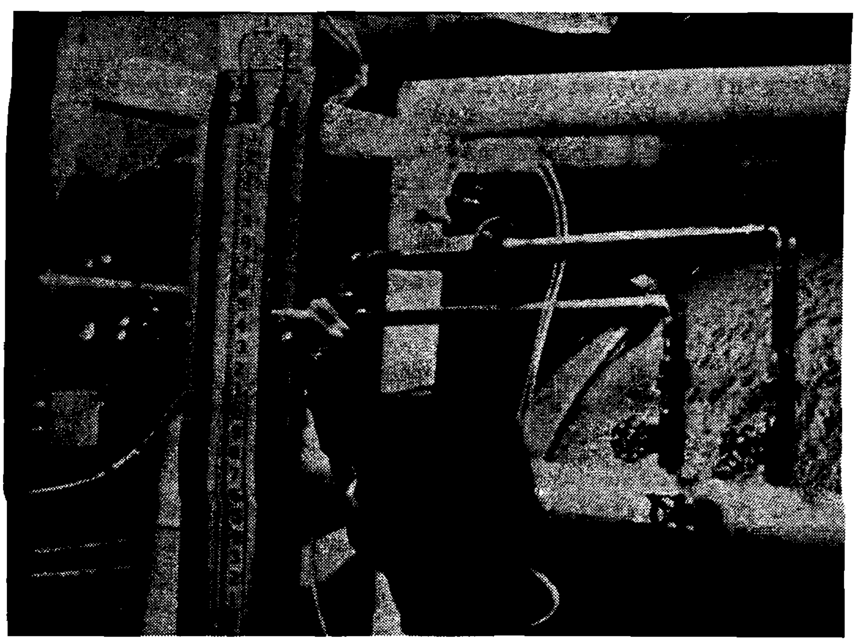

Figure 27.
Mass balance calibration rig for liquid flow meters.

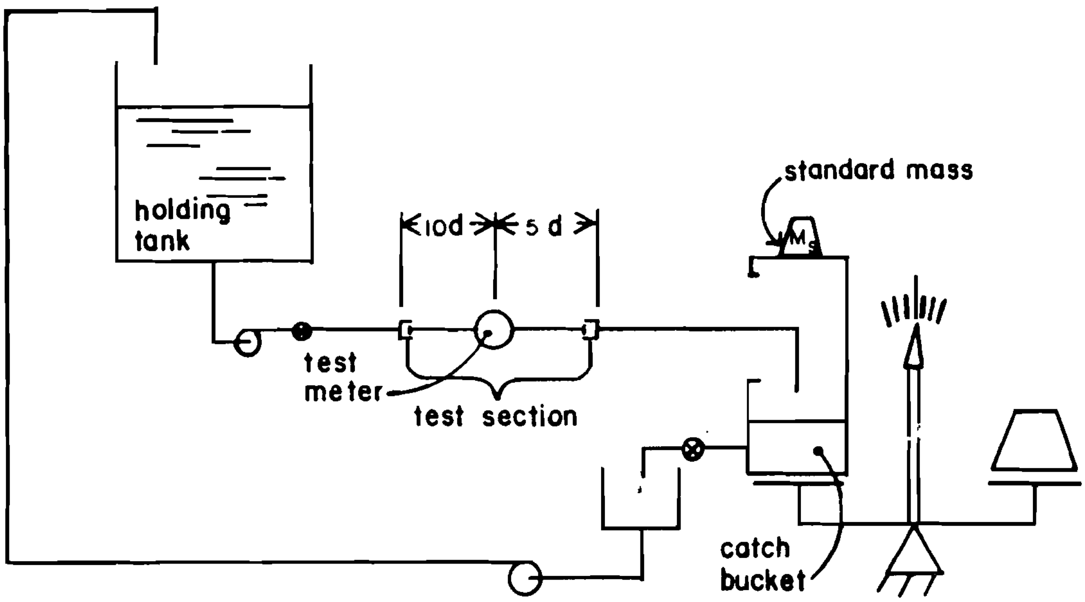

Figure 28.
Venturi meter and manometer used for in-situ calibration of turbine meters.

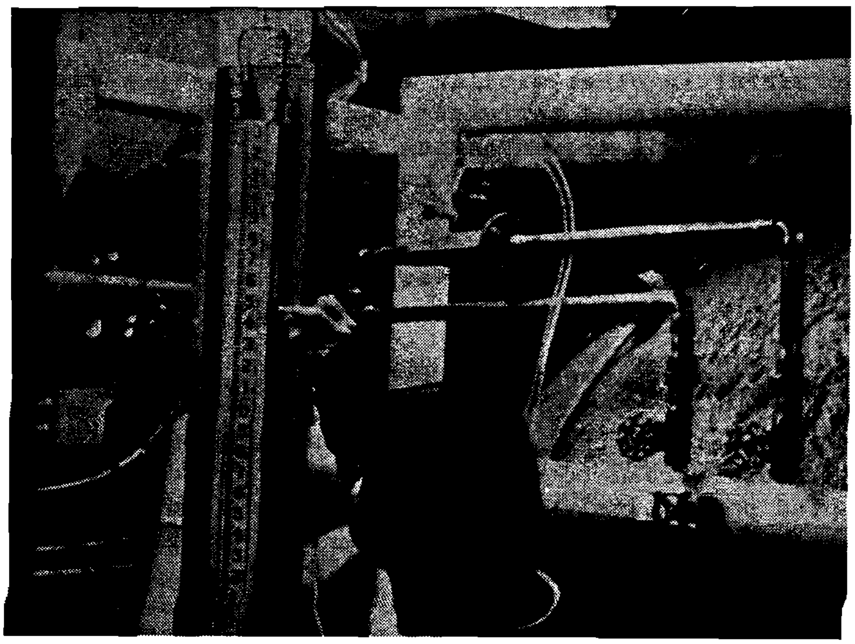

4. flow transients: the meter does not experience flow transients during calibration;

5. weighing dynamics: the mass on the balance is the same at the end of the run as at the beginning - the balance indicator will therefore cross zero at the same speed.

A dump spigot on the weighing bucket and a sump to return fluid to the holding tank expedites multiple calibration runs.

An in-situ calibration procedure that is more convenient than the mass balance calibration procedure has recently been adopted. Valves and unions are installed downstream of the turbine meter so that a venturi meter can be connected in series as shown in Figure 28. Low cost aluminum venturis have proven suitable because they are only used for short periods of time. The venturi meter is calibrated using the mass balance apparatus described previously.

The advantages of this procedure are that the test meter is calibrated with the same fluid and flow geometry as is used during performance monitoring and with the same signal conditioning modules that are used during performance monitoring. In other words, a "system calibration" is performed. The calibrations are also performed more quickly and therefore more frequently by the in-site procedure than by the mass balance procedure.

Conclusions

The objectives to continuously and accurately monitor the performance of full scale solar heating and cooling systems for residential buildings have been met. Special purpose measurement systems and calibration procedures have been developed at CSU to meet these objectives at reasonable cost. The techniques presented here are based on accepted measuring principles and should be useful in other similar applications. However, little has been said about data logging equipment and micro-computers for data reduction. These technologies are advancing so rapidly that by the time one has received, connected, programmed, and reported on one's system it is generally obsolete. Obsolete or not, the dedicated micro-computer systems that have been used for real time data reduction at CSU for the past seven years have been essential to the success of the projects and will continue to be so.

Appendix A: Analysis of Temperature Probe Errors

A thermocouple probe (or other temperature sensing probe) is normally immersed in a fluid stream to measure the local fluid temperature. The probe is coupled convectively to the fluid and conductively (along its length) to the wall on which it is mounted. If the fluid is a gas, such as air, the probe is also coupled radiatively to the walls which it can see. The duct or pipe wall temperature often deviates substantially from the temperature of the bulk of the fluid. With electrically excited temperature sensors there is also a self-heating effect produced by the resistance heating of the probe tip. To properly design temperature probes, the biases produced by the radiation, conduction and self-heating effects are estimated using the relations derived by deWinter [3], which are summarized below.

Radiation Effect

Let us assume that the probe is immersed in a fluid of uniform temperature T_f, and that the wall is at a uniform temperature T_w.

The steady-state radiation error, defined as the difference between the sensor temperature, T, and T_f, is given by

$$\Delta T_{rad} \equiv (T - T_f) = (T_w - T)\ h_{rad}/h_{conv}$$

The convection heat transfer coefficient, h_{conv}, is primarily a function of the fluid properties, velocity and probe size. With smaller probe size, h_{conv} normally increases so that the error in the reading becomes less. Empirical relations for estimating h_{conv} are given by McAdams [9] for the case of flow normal to a cylindrical probe of diameter D:

$$\frac{h_{conv}D}{k} = 0.32 + 0.43\ (\frac{\rho VD}{\mu})^{0.52} \qquad \text{for } 0.1 < (\frac{\rho VD}{\mu}) < 1000$$

and

$$\frac{h_{conv}D}{k} = 0.24\ (\frac{\rho VD}{\mu})^{0.60} \qquad \text{for } 1000 < (\frac{\rho VD}{\mu}) < 50{,}000$$

where

V = velocity of the fluid, (ft/hr)
k = conductivity, W/mK (btu/ft F hr)
ρ = density, kg/^{3} (lbm/ft^3)
μ = viscosity, kg/ms (lbm/ft hr)

The radiation heat transfer coefficient, h_{rad}, for a probe with a perimeter very small compared to the perimeter of the flow passage is normally well approximated by:

$$h_{rad} \simeq \varepsilon\sigma\ (\frac{T_f + T_w}{2})^3$$

where ε is the emissivity of the probe and $\sigma = 5.669 \times 10^{-8}$ w/m K^4 (.1714 x 1^{-8} Btu/ft^2 hr) F^4 is the Stephan-Boltzman constant.

Conduction Effect

If we consider a slender probe built into a wall (at temperature T_w) at one end, and immersed in a fluid (at temperature T_f) along its full length, with the fluid in turn surrounded by a wall (at temperature T_w), we can derive the standard fin differential equation (see any standard heat transfer text):

$$kA\frac{d^2T}{dx^2} - h_{conv}\ 2\pi r\ (T - T_f) - h_{rad}\ 2\pi r\ (T - T_w) = 0$$

This leads to the following expression for conduction error:

$$\Delta T_{cond} = T - T_f = (T_w - T_f)\,\frac{1}{\cosh mL} = (T_w - T\,)\,\frac{1}{\cosh mL - 1}$$

where

$$m = \sqrt{\frac{(h_{rad} + h_{conv})\pi D}{kA}},$$

and where T is the temperature at the tip of the probe, L is the length of the probe, and kA is the probe's overall axial conductance; i.e. the sum of all the conductivity-area products in the cross section of the probe.

Self-Heating Effect

If an RTD or semiconductor sensor is used heat is generated because of the power, Q, dissipated by the excitation current and sensor voltage drop. This raises the measured temperature above the temperature which would otherwise be sensed. The standard fin equation results (for the conditions of the self heating problem) in the expression for self heat error:

$$\Delta T_{self} = \frac{Q \tanh mL}{\sqrt{Ak\ (h_{rad} + h_{conv})\ 2\pi r}}$$

The overall probe error is therefore given by

$$T - T_f = (T_w - T)\left[\frac{h_r}{h_c} + \frac{1}{\cosh mL - 1}\right] + \frac{Q \tanh mL}{\sqrt{Ak\ (h_r + h_c)\ \pi D}}$$

This expression gives T_f in terms of T_w and the biased temperature reading, T. For estimating the error in order to design or select a probe, an iterative procedure must be used to solve for T in terms of T_w and T_f.

One should also estimate the probe's time constant. The following approximation is only slightly conservative:

$$\tau = A\rho c_p/(h_r + h_c)\pi D$$

where $A\rho c_p$ is the probe's thermal capacitance per unit length; i.e. the sum of all specific heat-density-area products in the cross section of the probe. The probe should be designed to have a time constant, τ, that is less than 10% of the scan interval.

An example calculation of temperature probe error appears in [3].

References

1. G.O.G. Lof, et.al.: "Performance of Eight Solar Heating and Cooling Systems in CSU Solar House I, 1980-1981," Final Report COO-30122-27 (SAN-30569-14) Solar Energy Applications Laboratory, Colorado State University, Fort Collins, CO, June, 1982.

2. S. Karaki, et al.: "Performance Evaluation of a State-of-the-Art Solar Air Heating System with Auxiliary Heat Pump,' Final Report COO-30122-4, SEAL, CSU, Fort Collins, CO, January 1980.

3. Altas Corporation: "Monitoring the Performance of Solar Heated and Cooled Buildings," Volume 2: "Measuring Instruments," EPRI ER-1239 Final Report, Palo Alto, CA, November 1979.

4. NBS: "Thermocouple Reference Tables Based on IPTS-68," National Bureau of Standards Monograph 125, Washington, D.C., March 1974.

5. S. Karaki and P. R. Armstrong: "Instrumentation, Data Acquisition and Monitoring Systems for an Air Heating Solar System," Conf. on Performance Monitoring Techniques for Evaluating Solar Heated and Cooled Buildings, R. Boehm, Ed., Washington, D.C., April 1978.

6. ASHRAE: "Methods of Testing for Rating Room Air Conditioner Heating Capacity," Standard 58-65, American Soc. of Heating, Refrigeration and Air Conditioning Engineers, 345 East 47th Street, New York, NY 10017, 1965.

7. ASHRAE: "Methods of Testing for Rating Unitary Air Conditioning and Heat Pump Equipment," Standard 37-69, 1969.

8. NBS: "Development of Proposed Standards for Testing Solar Collectors and Thermal Storage Devices," Technical Note 899, National Bureau of Standards, Washington, D.C., Feb. 1976.

9. W.H. McAdams: Heat Transmission, 3rd ed., McGraw-Hill, New York, 1953.

SERI/CP-281-2173
DE84000027
UC Category: 59c

Performance Monitoring of Active Solar Energy Systems

Proceedings
of the
Second National Workshop
January 20-21, 1983
at the
Florida Solar Energy Center

Sponsored by:
U.S. Department of Energy
Office of Solar Heat Technologies
and the
Solar Energy Research Institute

Edited by:
Marvin Yarosh
Associate Director
Florida Solar Energy Center
300 State Road 401
Cape Canaveral, Florida 32920

Printed and Distributed by:
The Solar Technical Information Program

Subcontract No. AY-2-02047-1
FSEC-CR-78-83 (EI)
June 1983